Preprint Title Local photocurrents in two dimensional materials measured by conductive atomic force microscopy

Authors Borislav Vasić

Publication Date 21 Jun 2022

Article Type Full Research Paper

ORCID® iDs Borislav Vasić - https://orcid.org/0000-0002-1575-8004

Local photocurrents in two dimensional materials measured by conductive atomic force microscopy

Borislav Vasić*

Address: Institute of Physics Belgrade, University of Belgrade, Pregrevica 118, 11080 Belgrade, Serbia

Email: Borislav Vasić - bvasic@ipb.ac.rs

* Corresponding author

Abstract

Local photocurrents are commonly measured by photoconductive atomic force microscope (PC-AFM) which consists of standard conductive AFM (C-AFM) coupled with an external light source. Here we demonstrate that even basic C-AFM setup without external light sources and equipped with a built-in red laser aimed for AFM feedback loop is sufficient in order to measure local photocurrents of two dimensional (2D) materials. In this study, WS_2 is taken as a test sample and typical representative of transition metal dichalcogenide based 2D semiconductors. We consider current-voltage characteristics and temporal response (current versus time) measured at single point as well as 2D current maps. Measurements are always performed for two cases, the AFM laser switched off and on, which correspond to dark and photocurrents, respectively. The special attention is devoted to the measurements of dark currents since they have to be done with AFM laser switched off. In that context, we demonstrate that only two-pass C-AFM provides stable scanning and current mapping. Although the presented approach provides a simple way to measure local photocurrents in 2D materials at the nanoscale, it inevitably has limitations which are discussed in detail.

Keywords

conductive atomic force microscopy; photocurrent; two dimensional materials

Introduction

Photodetection is one of the basic operations of optoelectronic devices where an incident light is transformed into an electrical signal - photocurrent. The photodetection is usually based on two effects [1]. In the photoconductive effect, photocurrents are induced by the light with the energy exceeding electronic band gap. Such light excites electron-hole pairs which are separated by externally applied bias voltage and which constitute photocurrent. On the other hand, in the photovoltaic effect, the electric field needed for the separation of electron-hole pairs is not applied externally, but it is provided by the internal field of p-n junctions.

Two dimensional (2D) materials and related van der Waals heterostructures are attractive for the fabrication of a new generation of photodetectors [1-5]. The 2D materials are associated with a broad range of energy band gaps and therefore they can provide photodetectors operating in a wide spectral range, from far-and mid-infrared, to near-infrared, visible, and ultraviolet region. Since they are atomically thin, the corresponding photodetectors are very compact. At the same time, strong light-matter interaction in 2D materials enables very efficient photodetection. In addition, 2D materials are generally very elastic which allows design of flexible photodetectors.

2D photodetectors are commonly characterized by macroscopic I/V measurements. Still, in order to further elucidate physics behind these devices, it is necessary to relate their optoelectronic properties with their structure and morphology. Therefore, microscopic characterization and measurements of local photocurrents could bring novel insights about the influence of spatial variations in 2D materials on photodetectors' performance. Scanning photocurrent mapping systems [6-9] allow the measurement of spatial photocurrent maps of 2D materials, but the spatial resolution is determined by the size of a laser spot, that is by the diffraction limit. Since electrical properties of 2D materials are strongly influenced by local inhomogeneities (grain boundaries, wrinkles, bubbles, non-uniform thickness due to varying number of layers) [10-16] with nanoscale dimensions (far below the diffraction limit), microscopic techniques with better resolution are needed. In conductive atomic force microscopy (C-AFM) [17-19], a conductive AFM probe with nanometric dimensions, acts as a sharp and moveable electrode. It scans the sample surface in contact mode with simultaneously applied bias voltage. As a result, current maps are measured with the nanoscale resolution. C-AFM has been successfully employed for the investigation of local electrical properties of 2D materials, graphene, transition metal dichalcogenides (TMDs) and related heterostructures [15,16,20-35], as well as for studies of dielectric properties and breakdown of 2D insulators such as hexagonal boron nitride [36-38]. Photoconductive AFM (PC-AFM) is a variant of C-AFM aimed for studies of photoconductive materials [39,40]. Here, local photocurrent is measured while an external light source is focused on the AFM tip-sample contact. This technique has been also used in order to study the photoresponse of 2D semiconductors [41-45]. Interestingly, common C-AFM setup (without any external light source) already contains an internal light source - AFM-feedback laser. Therefore, even basic C-AFM setup is equipped with a light source which can be strong enough to induce photocurrents as already observed on bulk semiconductors and nanostructures [46-50] and recently on 2D/3D heterostructure made from graphene and silicon [51].

The aim of this paper is twofold. First we demonstrate that basic C-AFM setup equipped only with a red AFM-feedback laser is efficient tool for the measurement of local photocurrents of 2D TMDs with the nanoscale resolution. This is illustrated by measuring local I/V curves and temporal response (curent versus time) at single point, as well as by measuring current maps of WS_2, selected as a typical representative of TMD based 2D semiconductors. The main issue with this approach is how to measure dark current. The answer on this question is the second aim and we demonstrate two methods: 1. C-AFM with switched off AFM-feedback laser and inactive feedback loop, and 2. C-AFM realized as a two-pass technique.

Results and Discussion

AFM laser adjustment

Optical images (the top view) of the AFM cantilever above WS_2 flake with the AFM laser switched on and off are displayed in Figs. 1(a) and 1(b), respectively. In a standard configuration, the AFM laser is focused onto the AFM cantilever and further reflected back onto four-segment photodiode.

Since the cantilever covers the AFM tip, it prevents focusing of the laser light at the tip-sample contact. Still, as can be seen from Fig. 1(a), a significant part of the laser light is randomly scattered around the cantilever and falls down onto sample surface [48]. The red AFM laser operates at 650 nm which corresponds to the energy of around 1.9 eV. This energy is larger than the band gaps of most frequently used TMDs, MoS_2, $MoSe_2$, WS_2, WSe_2, [52-54], which are most promising 2D semiconductors for photodection [1-5,52,54]. Therefore, the red light scattered from the AFM cantilever can excite electrons from the valence to the conduction band of WS_2 considered in this study. If the mean free path of photo-induced charge carriers is larger than the distance between the AFM tip and the point where the scattered light falls onto the WS_2 surface, photocarriers could reach the AFM tip and constitute photocurrent.

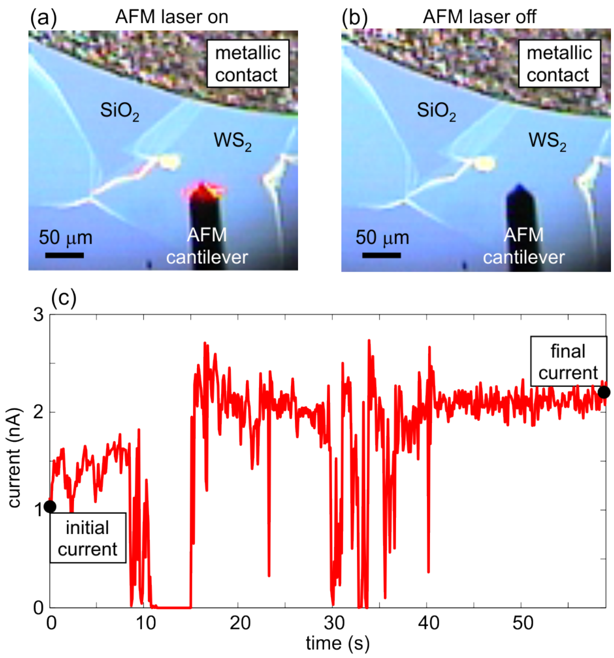

Figure 1: The top view of the AFM cantilever with the red AFM laser switched (a) on and (b) off. The image also displays WS_2 grown on SiO_2/Si substrate. The electrical contact to the WS_2 flake was made by silver paste depicted at the top-right corner. (c) Temporal response of the current measured by the AFM tip during the AFM laser adjustment. The applied bias voltage was 5 V.

In addition to the internal AFM laser, our AFM system is equipped with a white-light LED lamp commonly used for the illumination of AFM cantilever and sample. Although this is an external light source, it is an integral part of most AFM systems. Therefore it was also considered as a light source in this study. When both light sources, the AFM laser and lamp, are switched on, the total current consists of three terms: 1. dark current I_{dark} which stands for the current measured without any light source, 2. the photocurrent induced by the LED lamp I_{lamp}, and 3. the photocurrent induced by the AFM laser I_{laser}.

Prior to common AFM measurements, the AFM laser should be focused onto the cantilever so that the intensity of the reflected light on the four-segment photodiode is maximized. On the other hand, if the AFM is intended as a light source for photoconductive measurements, the procedure for the AFM laser alignment should be modified. In our study, as a first step, the intensity of the reflected laser light falling onto the four-segment photodiode was maximized as usually done. Then the AFM tip approached the sample surface in contact mode and bias voltage was applied to the sample. Since the aim was to maximize photocurrent, it was necessary to maximize the light randomly scattered around the AFM cantilever. For that purpose, after the approach, the whole platform with the AFM chip and cantilever was moving laterally, while changes of the current through the AFM tip were being followed simultaneously in a real time. The movement of the AFM cantilever corresponds to relative motion of the AFM laser. Typical results of the adjustment procedure are depicted in Fig. 1(c) showing variations in photocurrent during the lateral movement of the AFM cantilever. The optimal position of the AFM cantilever (AFM laser) is the one which gives the maximal photocurrent. As can be seen from Fig. 1(c), the final current (around 2 nA) is doubled the initial current (around 1 nA). Since the dark current and photocurrent induced by the LED lamp are constant and independent on the position of the AFM cantilever (its relative position to the AFM laser), by maximizing the total current, we maximize the photocurrent induced by the AFM laser.

Large current oscillations observed in Fig. 1(c) stem from the movement of the AFM laser. The intensity of the reflected light on the four-segment photodiode is then continuously varying. Since this is the input signal for the AFM feedback loop, its variations inevitably cause instabilities in the vertical position of the AFM tip (sample) thus resulting in current oscillations. They cannot be avoided, but in order to minimize the observed instabilities, the lateral movement of the AFM chip should be done slowly.

In addition to photocurrent measurements, the characterization of photoconductive materials requires measurements of dark current. This is straightforward in systems with an external light source since in that case, it is just necessary to switch off the external light. However, dark current measurements are not trivial if the AFM laser is used as a light source. Namely, the main issue when the AFM laser is switched off is how to provide stable vertical position of the AFM tip (in fact, the vertical position of the scanner, since our system is based on scanning by a sample, therefore, the AFM tip is fixed, while the scanner holding the sample is moving both in lateral and vertical direction). When the AFM tip is in contact with a sample, the AFM cantilever is bended and its deflection is regulated by the set point SP_0 which regulates the normal force applied by the tip. If the AFM laser is switched off, the control system interprets this as an abrupt drop of the deflection signal from SP_0 to zero. Then the control system will try to reestablish the predefined set-point (deflection of the AFM cantilever) by moving the scanner (with the sample) up, toward the AFM tip. Since they were already in the contact, further vertical movement of the sample will cause a crash and tip damage. In order to avoid this scenario, before the AFM laser is switched off, we first turn off the feedback loop by setting all gains of the feedback-loop amplifier to zero. Then, the AFM feedback loop is inactive while the vertical position of the AFM scanner is fixed.

Single-point measurements

Temporal response

Current measured by C-AFM at single point as a function of time is illustrated in Fig. 2(a). The current intensity was controlled by switching light sources, while the temporal response was measured with AFM feedback loop turned off (feedback gains set to zero). At the initial moment, both the AFM laser and lamp were switched on and the resulting current was I_0. At $t \approx 10$ s, the lamp was switched off and the current decreased to I_1. Finally, at $t \approx 20$ s, the laser was switched off as well, and the current felt down to I_2. The current measured without any light source is dark current $I_{\text{dark}} = I_2$. Difference $I_{\text{laser}} = I_1 - I_2$ corresponds to the photocurrent induced by the AFM laser.

Finally, the photocurrent generated by the lamp is equal to the difference between the total current and the sum of the dark current and the photocurrent induced by the AFM laser, $I_{lamp} = I_0 - I_1$.

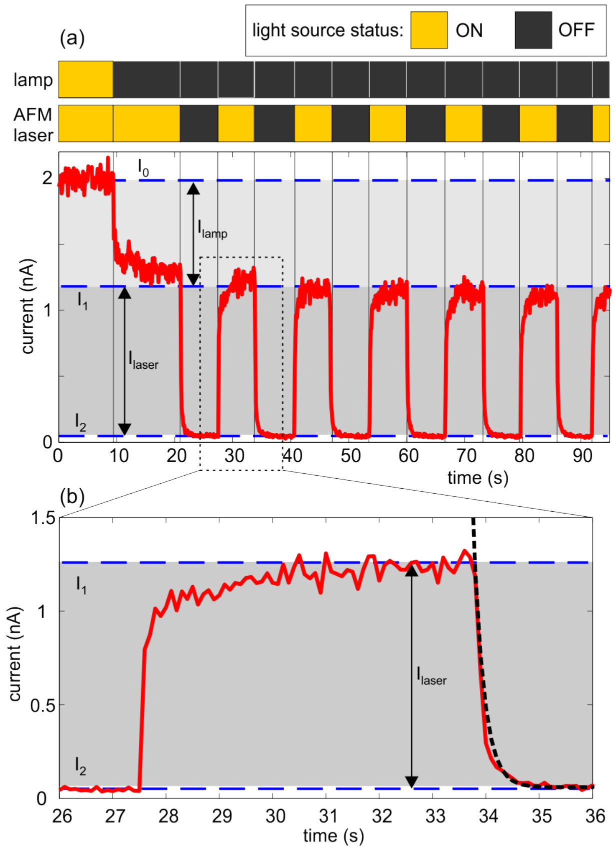

Figure 2: (a) Temporal response of the switching process: current through the AFM tip (measurements at single point) as a function of time and for different status of light sources, the AFM laser and LED lamp. (b) Current evolution during single switching cycle. The applied bias voltage was 5 V.

For $t > 20$ s, the graph in Fig. 2(a) illustrates several cycles where the current was modulated between two levels, I_1 and I_2, which was achieved by switching the AFM laser on and off (the lamp was switched off). As can be seen, the switching process was well controlled. Still, current I_1 decreased with time, which is obvious if we compare the intervals 10-20 s and 80-85 s, where the measured current was $I_1 \approx 1.3$ nA and $I_1 \approx 1.1$ nA, respectively. The decrease of I_1 was an enduring process and almost linear with time which indicates slow but continuous degradation of tip-sample contact. This was not surprising since the measurements were done with inactive feedback loop (further discussion given in section where the photocurrent mapping by single-pass C-AFM is analyzed).

In order to better emphasize temporal dynamics of the switching process, single cycle is zoomed in Fig. 2(b). As can be seen, the current profile is associated with rise and fall times when the laser is switched on and off, respectively. The rise (fall) time can be defined as a time interval where the current rises (falls) from I_1 to I_2 (I_2 to I_1) when the laser is switched on (off). The current within these time intervals changes exponentially. This is illustrated for the fall time in Fig. 2(b), where the current was fitted by an exponential function $I_2 + (I_1 - I_2)\exp(-(t - t_0)/\tau)$, where t_0 corresponds to the moment (around 34 s) when the laser was switched off, whereas τ is a time constant. τ was determined by the fitting and it was in the range $150 - 200$ ms. Usually, the fall time is explained as a result of the photogating effect [55-58]. Namely, charge carriers in 2D materials are trapped by molecules adsorbed on or beneath 2D layers. As a result, recombination of the charge carriers is prolonged while the time required for the switching off (the transition from I_2 to I_1) is extended. Although number of trapped molecules strongly depends on environmental conditions (humidity, air or vacuum, bare or encapsulated 2D layers), the obtained values for the fall time were similar to those measured for MoS_2 based photodetectors [55].

Local I/V curves

I/V curves measured at single point of WS_2 flake and for the AFM laser switched on and off are presented in Fig. 3. During the measurement, the LED lamp was switched off, while the AFM feedback loop was inactive. I/V curve measured for the laser switched off represent dark current. On the other hand, the current measured for the laser switched on is significantly enhanced, while the voltage threshold is reduced (from $\sim$ 6 V for the laser switched off to $\sim$ 2 V for the laser switched on). The photocurrent as a function of bias voltage can be obtained as a difference between two curves.

It is well known that I/V measurements of 2D materials strongly depend on environmental conditions [59,60]. In order to illustrate this issue, the inset of Fig. 3 displays I/V curves measured in five successive cycles (each of them consists of forward and backward sweep direction) for both laser switched on and off. As can be seen, the curves exhibit a hysteresis in both cases. This is usually observed in I/V measurements done at ambient conditions, mainly due to various adsorbed

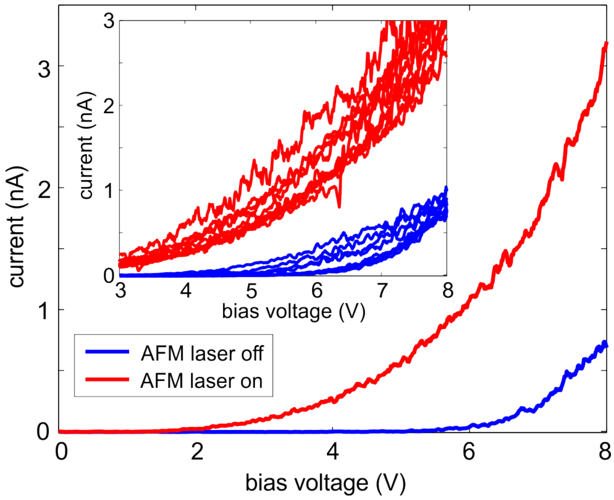

Figure 3: Selected I/V curves for the AFM laser switched on and off. All I/V curves measured in five successive cycles during sweeping bias voltage from negative to positive values and vice versa are presented in the inset.

molecules which act as trapping centers [59,60]. At the same time, the photogating effect can also contribute to the observed hysteresis [55-58,60]. Although the hysteresis and its origin are outside the scope of this manuscript, their influence on measured dark and photocurrents can not be neglected. As a result, both dark and photocurrents should be defined in a certain range around an average value. For example, at 7 V, the measured dark current is $\sim 0.45 \pm 0.25$ nA, while the current measured for the laser switched on is $\sim 2.1 \pm 0.6$ nA.

Current maps

Temporal response and I/V curves analyzed in the previous sections were measured at single point. The next step was to use C-AFM and scan the surface of WS_2 flakes in order to obtain 2D photocurrent maps. Two approaches are studied here based on single- and two-pass C-AFM.

Single-pass C-AFM

Single-pass C-AFM measurements were done in a similar way as previously measured temporal response and I/V curves, but with additional scanning in contact mode. Therefore, prior to C-AFM measurements, the feedback gain was set to zero and the feedback loop was inactive. This prevented any uncontrolled vertical movement of the AFM scanner and allowed safe dark current measurements done with the AFM laser switched off. Photocurrent maps were standardly obtained with the AFM laser switched on.

The current maps measured in forward and backward scan directions are depicted in Fig. 4(a). The status of light sources is indicated on the right hand side. The current mapping was started from the top, with the vertical direction as a slow-scan axis. The characteristic current profile along the vertical dashed line (for the current map measured in the backward direction) is displayed in Fig. 4(b). As can be seen, the current map consists of six stripes (1-6) which correspond to three characteristic current levels I_0, I_1, I_2 standing for dark current $I_{\text{dark}} = I_2$, photocurrent induced by the AFM laser $I_{\text{laser}} = I_1 - I_2$, and photocurrent generated by the lamp $I_{\text{lamp}} = I_0 - I_1$. The first four stripes 1-4 (from the top) correspond to the sequence $I_2 \rightarrow I_1 \rightarrow I_2 \rightarrow I_1$. Here the AFM laser was switched off-on-off-on, respectively, while the LED lamp was permanently switched off. Therefore, the difference between two current levels corresponds to the photocurrent induced by the AFM laser I_{laser}. In the fifth sequence, the lamp was switched on as well, which resulted in the maximal current level I_0.

The presented results illustrate that basic C-AFM setup with red AFM laser is enough in order to map dark and photocurrents in TMD based 2D semiconductors. Still, single pass measurements are associated with current oscillations which increase with time. They are represented in the current profile in Fig. 4(b). As can be seen, the current is smooth at the beginning of the scanning, in domains 1-4 (for small distance along slow-scan axis), but the oscillations become more pronounced with time, in domains 5 and 6 (for larger distance along slow-scan axis). This effect is further illustrated in Fig. 4(c) with current profiles from the second and sixth stripes (dotted lines 1 and 2, respectively, from the current map in 4(a) measured in the backward direction). In both cases, the AFM laser is switched on, but current oscillations are much more pronounced in the sixth stripe (line 2) which was measured several minutes after the second stripe.

The observed current oscillations appear due to fixed sample height without automatic control of the tip-sample distance. As a result, the tip-sample contact is not stable and current oscillates. At the beginning of the scanning, the contact is well defined since the sample height is defined by the

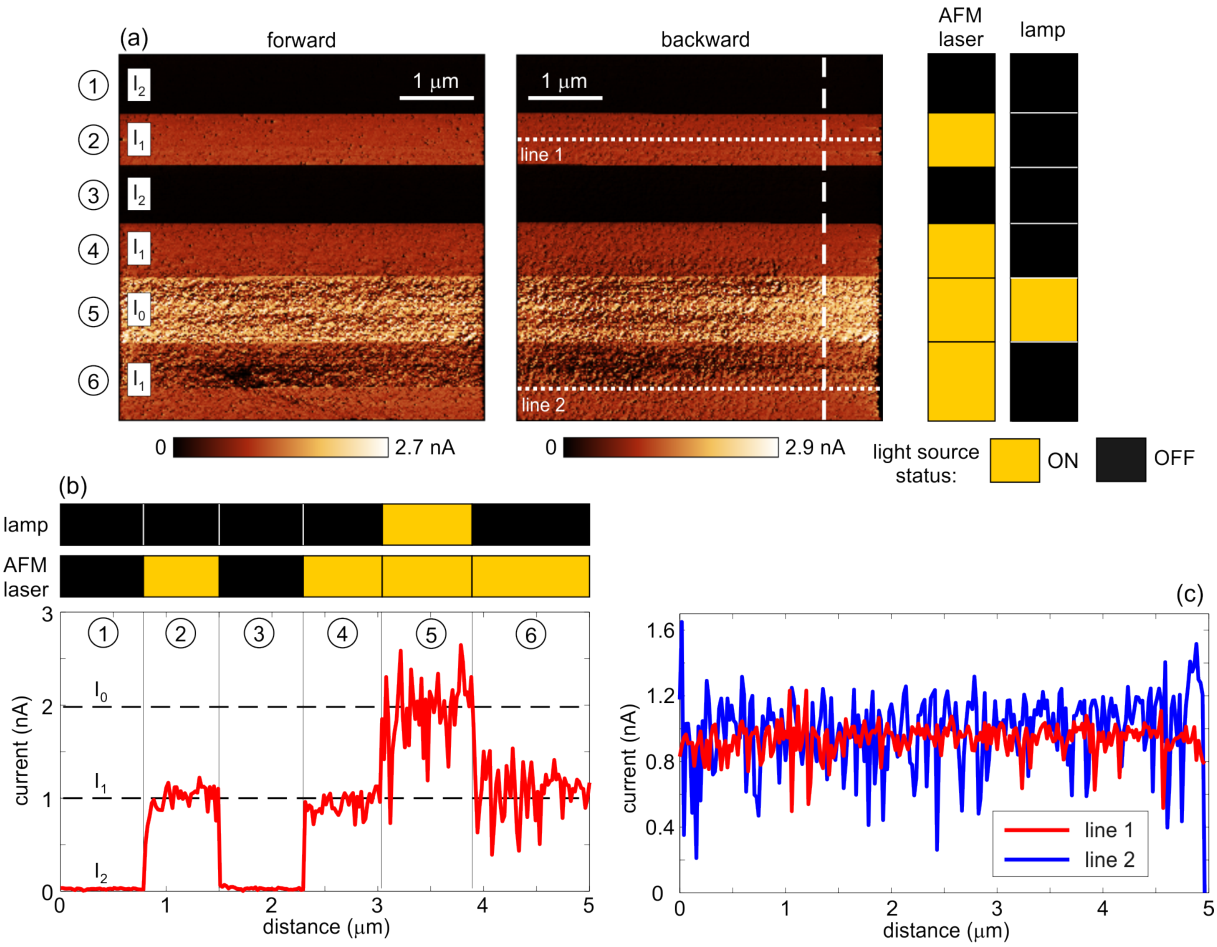

Figure 4: Single-pass C-AFM: (a) current maps measured on WS_2 flake in forward (left to right) and backward (right to left) scan directions, (b) current profile along vertical dashed line from the map in (a) (measured for the backward direction), and (c) current profiles along dotted lines 1 and 2 from the map in (a) (measured for the backward direction). The applied bias voltage was 5 V.

set-point used for the AFM tip approach, when the AFM feedback loop was still active. However, moving apart from this starting point and as time passes, the tip-sample contact degrades since any slope of the sample surface or local deviations in morphology such as holes or protrusions modify tip-sample interaction. Finally, too large deviations in the sample height could prevent safe scanning and result in severe damage of the AFM tip due to uncontrolled tip-sample force.

Single-pass C-AFM measurements are obviously feasible on samples with a relatively smooth surface. 2D materials certainly fall into this group, although they are usually associated with residues appeared during fabrication process, bubbles formed during transfer on a desired substrate, and various adsorbates from environment. Still, different procedures for post-fabrication treatments and cleaning have been developed and can be applied prior to C-AFM measurements in order to make surface of 2D materials as flat as possible. In addition, the intrinsic slope of underlying substrate (here SiO_2/Si) should be taken into account. In standard measurements, its effect is canceled in a real time by the work of AFM feedback loop and by image post-processing, for example by plane correction in order to subtract constant sample slope. Still, in the case of single-pass C-AFM with inactivated feedback-loop, the intrinsic substrate slope limits the sample area where scanning is stable and safe.

In addition to observed current oscillations and instabilities, another drawback of single-pass measurements is that topographic measurements are not feasible. The height signal, or more precisely, the signal obtained from the height channel, which was measured simultaneously with the previous current maps, is displayed in Fig. 5(a). Bright contrast (maximum) in the middle and dark contrast (minimum) at corners indicate parabolic function. The parabolic dependence of the measured signal is further illustrated in Fig. 5(b) showing a three dimensional profile and Fig. 5(c) with profiles along x- and y-axis. The situation when the feedback loop is turned off corresponds to the scanning at a constant height, where the AFM tip is fixed, while the sample (scanner) is just moved laterally with fixed vertical height as schematically illustrated in the inset of Fig. 5(c). In this case, measurable quantity is proportional to the deflection of the AFM cantilever which is proportional to the tip-sample interaction force, but not to sample topography. The parabolic profile of the measured signal indicates that the interaction force is maximal in the middle and decreases as sample is moved to left or right. Namely, the lateral movement of the scanner with fixed height (fixed bias voltage responsible for the vertical extension/contraction of the scanner) corresponds to the contraction of the scanner tube at one side and extension of the tube at the other side, and vice versa (schematically illustrated in the inset of Fig. 5(c)). As a result, the scanner tube scans along a parabola and not along a flat line. Then the tip-sample distance increases when scanner tube moves toward edges of predefined scan area, which leads to decreased interaction force.

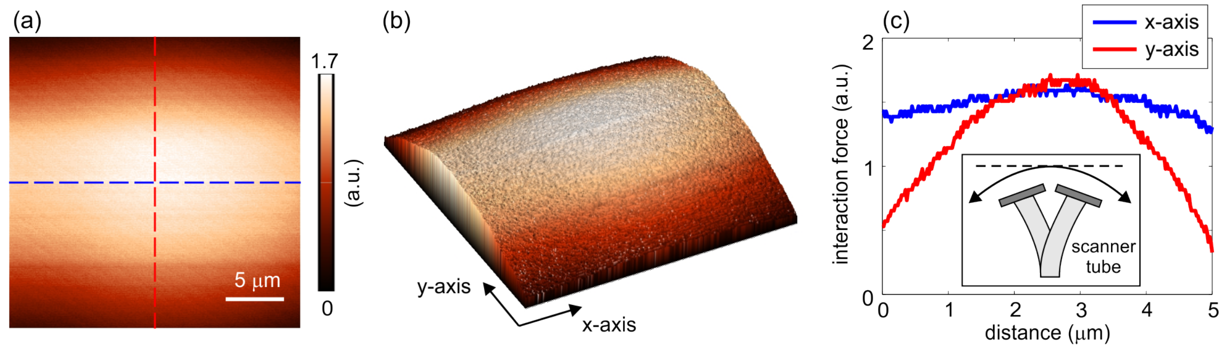

Figure 5: Signal which corresponds to tip-sample interaction force, obtained from the height channel and measured simultaneously with the current maps in Fig. 4(a): (a) two dimensional map, (b) three dimensional profile, and (c) one dimensional profiles along dashed lines in (a). The inset in (c) schematically depicts scanner movement along a parabola and not along a flat line.

Two-pass C-AFM

In order to overcome limitations of single-pass C-AFM, photocurrent measurements based on two-pass C-AFM were also analyzed. In the first pass, the AFM laser was switched on and the feedback loop was active. The scanning was done in contact mode while topography and photocurrent were measured simultaneously. Then, in the second pass, the AFM tip went along the same topographic line measured in the first pass. It should be emphasized that the tip was not lifted during the second pass as commonly done in other two-pass techniques, such as Kelvin probe force microscopy and magnetic force microscopy, in order to avoid van der Waals interaction between the AFM tip and sample surface. Therefore, in the second pass, the tip was still in contact with WS_2. Still, the difference compared to the first pass was that the AFM laser was switched off which allowed dark current measurements.

The current maps measured in the first and second pass are depicted in Figs. 6(a) and 6(b), respectively. They correspond to previously defined current levels I_1 (AFM laser switched on, lamp switched off) and I_2 (AFM laser switched off, lamp switched off), respectively. Histograms of two current maps in Fig. 6(c) reveal two peaks while their difference stands for an average photocurrent induced by the AFM laser $I_{laser} = I_1 - I_2$.

Photocurrent induced by the LED lamp was measured in a similar way. After the first pass where both the laser and lamp were switched on, in the second pass, the laser was switched off, the lamp

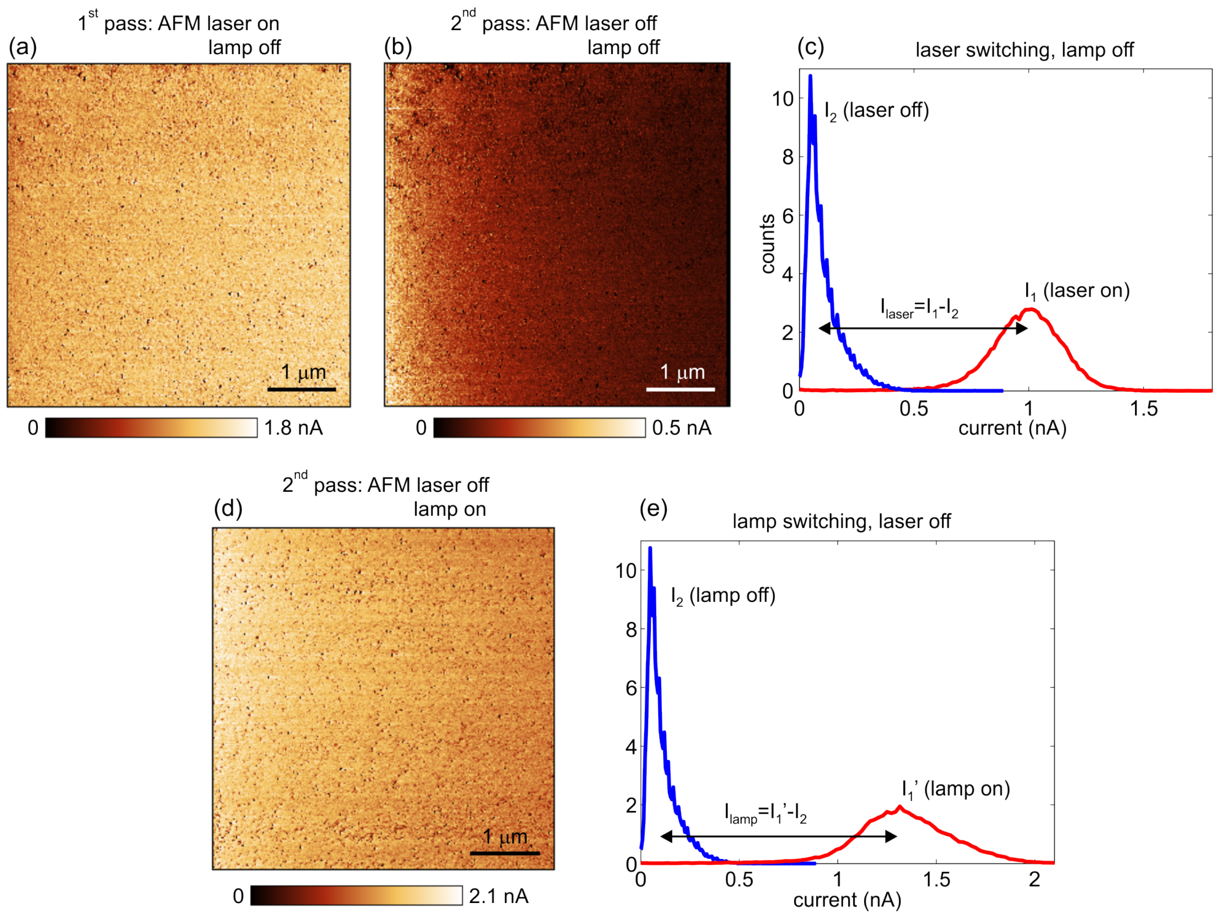

Figure 6: Two-pass C-AFM with the AFM laser switching (the LED lamp switched off): (a) current map measured in the first pass with the AFM laser switched on, (b) current map measured in the second pass with the AFM laser switched off, and (c) histograms of the current maps from (a) and (b). Two-pass C-AFM with the LED lamp switching (the AFM laser switched off): (d) current map measured in the second pass with the AFM lamp switched on and (e) histograms of the current maps from (b) and (d).

stayed switched on, while the scanning was repeated along same topographic lines without lifting of the AFM probe. The current map measured in the second pass and corresponding histogram are given in Figs. 6(d) and 6(e), respectively. The measured current represents level I_1' equal to the sum of dark current and photocurrent induced by the lamp (in previous notations, I_1 stands for a photocurrent obtained for AFM laser switched on and lamp switched off, here the situation is inverse and this is the reason why the prime sign was added). Difference between I_1' and dark current (measured in the second pass from the previous case in Fig. 6(b)) stands for an average photocurrent generated by the lamp $I_{\text{lamp}} = I_1' - I_2$.

Although dark current measurements in the second pass are done with inactive feedback loop, stability of the measurements are provided by the scanning along a predefined path defined by the surface topography recorded in the first pass. Still, the mapping of dark current in the second pass depends on scan velocity. This issue is visible as a slightly brighter contrast in the current maps on the left hand side of Figs. 6(b) and 6(d) which indicates enhanced current. In order to further explore this issue, Fig. 7(a) displays the dark current measured in the second pass for the AFM laser switched off and with varying scan velocity. The scanning was done from the left to right with the slow scan axis along the vertical direction. The scan velocity was decreasing from the top to bottom of the scan area within four horizontal stripes (indicated in Fig. 7(a)) in the following way: 7.5 μm/s (0.67 s per line), 5 μm/s (1 s per line), 2.5 μm/s (2 s per line), 1 μm/s (5 s per line). As can be seen, the current enhancement on the left hand side is less pronounced for slower scanning. This is further illustrated in Fig. 7(b) depicting average current profiles recorded for different scan velocities. The current has a maximum at the left hand side and then slowly decreases with a distance (toward the right hand side), while the slope (the absolute value) of the current profiles decreases for lower scan velocity.

Points at the left hand side correspond to the transition from the first to the second pass and the switching the AFM laser off. As we have already observed in Fig. 2, the temporal response of the switching process is associated with a certain fall time (in the order of hundreds of miliseconds) due to the photogating effect and prolonged recombination of trapped charge carriers. The profiles in Fig. 7(b) with descending current illustrate the same thing. As scan speed decreases, the ratio between the fall time and the time needed for single scan line decreases as well. As a result, the current profile measured for 1 μm/s is almost a flat line. Another way to overcome this issue is to record current in the backward direction of the second pass which gives the system more time to enter into saturation.

Two-pass technique provides stable scanning since the AFM feedback loop is active and topographic measurements should be straightforward in principle. Still, the measurements of 2D materials in contact AFM mode are associated by tip-induced moving of adsorbates [61] and/or sur-

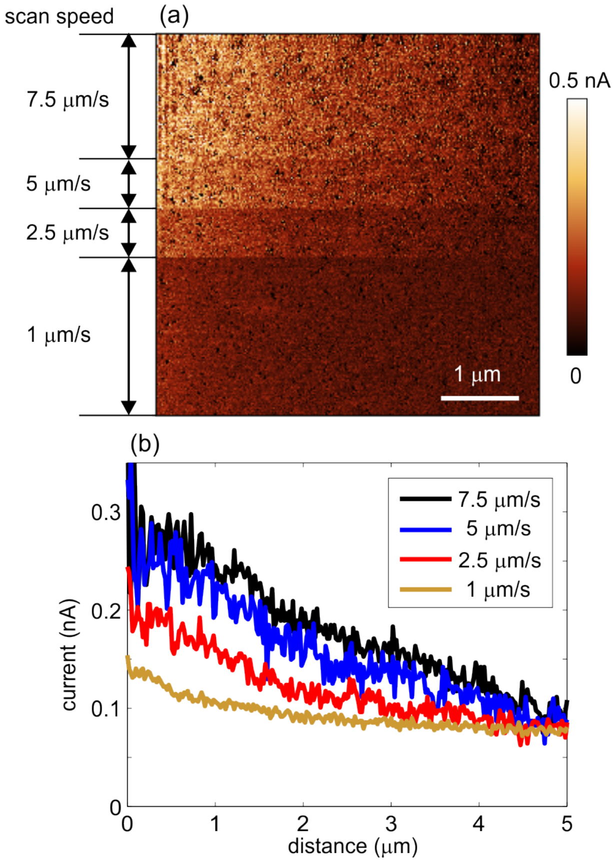

Figure 7: Dependence on scan velocity in two-pass C-AFM: (a) current map measured in the second pass with the AFM laser switched off and for different scan velocities, and (b) current profiles for different scan velocities. Every profile in (b) was obtained by averaging all profiles within a rectangular domain with indicated velocity in (a).

face flattening [16,62]. Figure 8(a) illustrates topography of WS_2 surface measured in the first pass. The array of bright lines appeared due to the moving of adsorbates from the WS_2 surface by AFM tip. After they had been partially removed in the first pass, they were less pronounced in the second pass as illustrated in Fig. 6(b). At the same time, the interaction between the AFM tip and adsorbates during C-AFM imaging could potentially lead to instabilities in current measurements as well. In that case, prior to C-AFM measurements, procedures for surface cleaning of 2D materials should be applied.

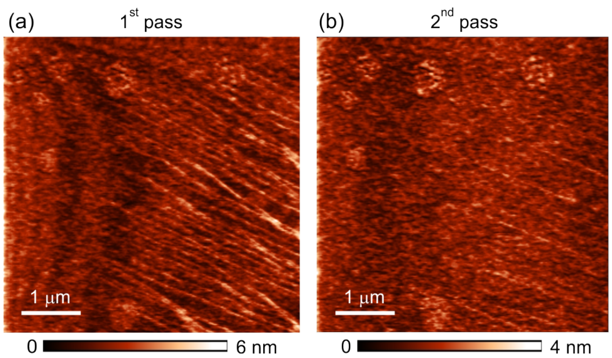

Figure 8: Morphology of WS_2 surface measured by two-pass C-AFM: (a) the first pass and (b) the second pass.

Discussion

The previous analysis demonstrates that C-AFM with red AFM laser employed as a light source is efficient tool for photocurrent measurements of 2D materials at the nanoscale. The presented methods are applicable in nanoscale studies of other semiconductors as well (not strictly 2D materials). Although simple, this approach has some inherent drawbacks and limitations. First, it is applicable only for materials with a bandgap E_{bg} similar or below the energy of the AFM feedback laser E_{laser}: $E_{\mathrm{bg}} \leq E_{\mathrm{laser}}$. As a result, AFM systems with red laser can be used for photocurrent measurements of 2D materials with bandgaps below $\sim$ 2 eV. TMD based 2D semiconductors, with a bandgap in the 1-2 eV range [52-54], obviously fall into this group. Still, measurements of wide-bandgap (larger than $\sim$ 2 eV) 2D semiconductors would not be possible. The bandgap threshold is further reduced in AFM systems with infrared feedback laser which makes these systems not suitable for photocurrent measurements using internal AFM laser.

While red AFM laser facilitates measurements of photocurrents, it makes difficult dark current measurements. Namely, such measurements have to be done with the AFM laser switched off which is not straightforward task as discussed above. Otherwise, if the AFM laser is switched on, the measured current inevitably comprises both dark and photocurrent. This should be taken into account in all C-AFM measurements of narrow-bandgap 2D semiconductors using AFM systems with red feedback laser. The same issue with dark current measurements will appear also in photocurrent measurements based on PC-AFM with external light sources (in the AFM systems with red feedback laser). In this case, dark current measurements should be done according to procedures described in this study.

Single point measurements done with inactive AFM feedback loop give reasonable results. They include temporal response and I/V curves measured at single point and for relatively short time period in the order of several seconds to tenths of seconds. Within this period, the contact between the AFM tip and sample stays relatively stable which provides reliable measurements of both dark and photocurrents. On the other hand, current mapping requires sample scanning and takes more time, in the order of several minutes. As demonstrated in Fig. 4, in the case of single-pass C-AFM done with inactive AFM feedback loop, the stability of current measurements degrades with time (also distance covered by AFM probe) resulting in significant current oscillations. On the other hand, two-pass C-AFM provides more stable results. Namely, photocurrents are measured with active AFM feedback loop, while during dark current measurements, AFM tip follows predefined path, measured in the first pass, which provides stable AFM tip-sample contact.

The presented measurements are based on switching AFM laser on and off. The frequency of the switching is not negligible in two-pass measurements. Therefore, if such measurements are going to be performed for long periods, care should be taken about lifetime of the laser and possible degradation of its performance. In our setup, currently there is no possibility for changing the output power of the AFM laser. Therefore, responsivity as a ratio between a photocurrent and input optical power cannot be measured.

Efficiency of photocurrent measurements based on AFM feedback laser was tested with top-visual conductive AFM probes (Pt coated VIT-P/Pt probes from NT-MDT) as well. Since their tip is not covered by the cantilever, we expected more light to be scattered around tip-sample contact and larger photocurrents. Two-pass C-AFM was used for the test, while prior to the measurements, the AFM laser was adjusted so that the photocurrent through the AFM tip was maximized, as described in section . Still, the ratio between average photocurrent and dark current $I_{\text{laser}}/I_{\text{dark}}$ was practically the same as the ratio obtained with standard AFM probes. Therefore, we could not achieve photocurrent enhancement with top-visual probes.

Conclusions

In a summary, local photocurrents in 2D materials with a bandgap below $\sim$ 2 eV can be efficiently measured with basic C-AFM setup, equipped with red AFM laser which is also used as a light source. The laser spot on the AFM cantilever should be adjusted so that the light scattered from the cantilever is maximized which gives the maximal current through the AFM tip. Photocurrent measurements are then routinely done since the AFM laser is switched on, while the AFM feedback loop is active. On the other hand, the main issues with this approach are dark current measurements which have to be done with the AFM laser switched off and inactive AFM feedback loop. Our results shows that single-point measurements of I/V curves and temporal response can be controlled sufficiently well even for the AFM laser switched off. Still, in order to maintain a stable current mapping on extended areas and for prolonged time periods, two-pass C-AFM is a prerequisite technique. Dark current is then measured in the second pass with the AFM laser switched off, while the AFM tip is moving along a trajectory defined by the topography line measured in the first pass, when the AFM feedback loop is active. The presented measurements methods are general and can be applied for other semiconducting materials as well.

Experimental methods

WS_2 layers were grown by chemical vapour deposition on SiO_2/Si substrate as described in our previous paper [16]. The electrical contact needed for C-AFM measurements was made simply by a silver paste (Figs. 1(a) and 1(b)). C-AFM measurements were done using Ntegra Prima system from NT-MDT and platinum coated probes CSG10/Pt from NT-MDT. During C-AFM measurements, the bias voltage was applied to WS_2 flake. The scanning was done in contact mode with simultaneous current measurements. I/V curves were measured at single points by sweeping bias voltage in the range $\pm$10 V. Temporal response was obtained by measuring current as a function of time (at single point as well) using built-in oscilloscope.

Internal AFM laser is used as a light source during C-AFM measurements. It is a standard part of the AFM feedback loop which controls tip-sample interaction. Ntegra Prima system is equipped with a red laser operating at 650 nm with a power of ∼ 0.5 mW. AFM systems are commonly equipped with an additional (external) light source, a lamp which is used in a combination with a CCD camera in order to make visible AFM cantilever and sample surface (as illustrated in Figs. 1(a) and 1(b)). In our system, white-light LED lamp coupled with 10x objective gives an average optical power of ~ 0.5 mW (0.32 mW at 650 nm, 0.52 mW at 533 nm, and 0.67 mW at 488 nm).

Acknowledgements

We acknowledge funding provided by the Institute of Physics Belgrade, through the grant of the Ministry of Education, Science, and Technological Development of the Republic of Serbia, and funding provided by the Science Fund of the Republic of Serbia, through the grant PROMIS 6062710 (PV-Waals). We are grateful to Davor Čapeta and Marko Kralj from the Center of Excellence for Advanced Materials and Sensing Device, Institute of Physics, Zagreb, Croatia, for providing us with WS_2 samples.

References

1. Buscema, M.; Island, J. O.; Groenendijk, D. J.; Blanter, S. I.; Steele, G. A.; van der Zant, H. S. J.; Castellanos-Gomez, A. *Chem. Soc. Rev.* **2015**, *44*, 3691–3718.

2. Koppens, F. H. L.; Mueller, T.; Avouris, P.; Ferrari, A. C.; Vitiello, M. S.; Polini, M. *Nat. Nanotechnol.* **2014**, *9*, 780–793.

3. Qiu, Q.; Huang, Z. *Adv. Mater.* **2021**, *33*, 2008126.

4. Wang, L.; Huang, L.; Tan, W. C.; Feng, X.; Chen, L.; Huang, X.; Ang, K.-W. *Small Methods* **2018**, *2*, 1700294.

5. Wei, X.; Yan, F.-G.; Shen, C.; Lv, Q.-S.; Wang, K.-Y. *Chin. Phys. B* **2017**, *26*, 038504.

6. Xia, F.; Mueller, T.; Golizadeh-Mojarad, R.; Freitag, M.; Lin, Y.-m.; Tsang, J.; Perebeinos, V.; Avouris, P. *Nano Lett.* **2009**, *9*, 1039–1044.

7. Britnell, L.; Ribeiro, R. M.; Eckmann, A.; Jalil, R.; Belle, B. D.; Mishchenko, A.; Kim, Y.-J.; Gorbachev, R. V.; Georgiou, T.; Morozov, S. V.; Grigorenko, A. N.; Geim, A. K.; Casiraghi, C.; Neto, A. H. C.; Novoselov, K. S. *Science* **2013**, *340*, 1311–1314.

8. Lee, C.-H.; Lee, G.-H.; van der Zande, A. M.; Chen, W.; Li, Y.; Han, M.; Cui, X.; Arefe, G.; Nuckolls, C.; Heinz, T. F.; Guo, J.; Hone, J.; Kim, P. *Nat. Nanotechnol.* **2014**, *9*, 676–681.

9. Reuter, C.; Frisenda, R.; Lin, D.-Y.; Ko, T.-S.; Perez de Lara, D.; Castellanos-Gomez, A. *Small Methods* **2017**, *1*, 1700119.

10. Xu, K.; Cao, P.; Heath, J. R. *Nano Lett.* **2009**, *9*, 4446–4451.

11. Zhu, W.; Low, T.; Perebeinos, V.; Bol, A. A.; Zhu, Y.; Yan, H.; et al., *Nano Lett.* **2012**, *12*, 3431–3436.

12. Tapasztó, L.; Nemes-Incze, P.; Dobrik, G.; Jae Yoo, K.; Hwang, C.; Biró, L. *Appl. Phys. Lett.* **2012**, *100*, 053114.

13. Clark, K. W.; Zhang, X.-G.; Vlassiouk, I. V.; He, G.; Feenstra, R. M.; Li, A.-P. *Nano Lett.* **2013**, *7*, 7956–7966.

14. Koepke, J. C.; Wood, J. D.; Estrada, D.; Ong, Z.-Y.; He, K. T.; Pop, E.; et al., *Nano Lett.* **2013**, *7*, 75–86.

15. Vasić, B.; Zurutuza, A.; Gajić, R. *Carbon* **2016**, *102*, 304–310.

16. Vasić, B.; Ralević, U.; Aškrabić, S.; Čapeta, D.; Kralj, M. *Nanotechnology* **2022**, *33*, 155707.

17. C., T.; I., B. Conductive Atomic-Force Microscopy Investigation of Nanostructures in Microelectronics. In *Scanning Probe Microscopy in Nanoscience and Nanotechnology 2. NanoScience and Technology*; B., B., Ed.; Springer, 2011; Chapter 23, pp 691–721.

18. *Conductive Atomic Force Microscopy: Applications in Nanomaterials*; Lanza, M., Ed.; Wiley-VCH, 2017.

19. Hui, F.; Lanza, M. *Nat. Electron.* **2019**, *2*, 221–229.

20. Li, Y.; Xu, C.-Y.; Zhen, L. *Appl. Phys. Lett.* **2013**, *102*, 143110.

21. Fu, D.; Zhou, J.; Tongay, S.; Liu, K.; Fan, W.; King Liu, T.-J.; Wu, J. *Appl. Phys. Lett.* **2013**, *103*, 183105.

22. Giannazzo, F.; Fisichella, G.; Piazza, A.; Agnello, S.; Roccaforte, F. *Phys. Rev. B* **2015**, *92*, 081307.

23. Lin, Y.-C.; Ghosh, R. K.; Addou, R.; Lu, N.; Eichfeld, S. M.; Zhu, H.; Li, M.-Y.; Peng, X.; Kim, M. J.; Li, L.-J.; Wallace, R. M.; Datta, S.; Robinson, J. A. *Nat. Commun.* **2015**, *6*, 7311.

24. Ruzmetov, D.; Zhang, K.; Stan, G.; Kalanyan, B.; Bhimanapati, G. R.; Eichfeld, S. M.; Burke, R. A.; Shah, P. B.; OÂ'Regan, T. P.; Crowne, F. J.; Birdwell, A. G.; Robinson, J. A.; Davydov, A. V.; Ivanov, T. G. *ACS Nano* **2016**, *10*, 3580–3588.

25. Quereda, J.; Palacios, J. J.; Agräit, N.; Castellanos-Gomez, A.; Rubio-Bollinger, G. *2D Mater.* **2017**, *4*, 021006.

26. Kaushik, V.; Varandani, D.; Das, P.; Mehta, B. R. *Appl. Phys. Lett.* **2017**, *111*, 141601.

27. Liu, J.; Goswami, A.; Jiang, K.; Khan, F.; Kim, S.; McGee, R.; Li, Z.; Hu, Z.; Lee, J.; Thundat, T. *Nat. Nanotechnol.* **2018**, *13*, 112–116.

28. Liao, M.; Wu, Z.-W.; Du, L.; Zhang, T.; Wei, Z.; Zhu, J.; Yu, H.; Tang, J.; Gu, L.; Xing, Y.; Yang, R.; Shi, D.; Yao, Y.; Zhang, G. *Nat. Commun.* **2018**, *9*, 4068.

29. Bampoulis, P.; Sotthewes, K.; Siekman, M. H.; Zandvliet, H. J. W. *ACS Appl. Mater. Interfaces* **2018**, *10*, 13218–13225.

30. Sotthewes, K.; van Bremen, R.; Dollekamp, E.; Boulogne, T.; Nowakowski, K.; Kas, D.; Zandvliet, H. J. W.; Bampoulis, P. *J. Phys. Chem. C* **2019**, *123*, 5411–5420.

31. Ludwig, J.; Mehta, A. N.; Mascaro, M.; Celano, U.; Chiappe, D.; Bender, H.; Vandervorst, W.; Paredis, K. *Nanotechnology* **2019**, *30*, 285705.

32. Li, R.; Taniguchi, T.; Watanabe, K.; Xue, J. *Rev. Sci. Instrum.* **2020**, *91*, 073702.

33. Giannazzo, F.; Schilirò, E.; Greco, G.; Roccaforte, F. *Nanomaterials* **2020**, *10*, 803.

34. Giannazzo, F.; Bosi, M.; Fabbri, F.; Schilirò, E.; Greco, G.; Roccaforte, F. *Phys. Status Solidi - Rapid Res. Lett.* **2020**, *14*, 1900393.

35. Vasić, B.; Ralević, U.; Cvetanović-Zobenica, K.; Smiljanić, M.; Gajić, R.; Spasenović, M.; Vollebregt, S. *Appl. Surf. Sci.* **2020**, *509*, 144792.

36. Lee, G.-H.; Yu, Y.-J.; Lee, C.; Dean, C.; Shepard, K. L.; Kim, P.; Hone, J. *Appl. Phys. Lett.* **2011**, *99*, 243114.

37. Hattori, Y.; Taniguchi, T.; Watanabe, K.; Nagashio, K. *ACS Nano* **2015**, *9*, 916–921.

38. Ji, Y.; Pan, C.; Zhang, M.; Long, S.; Lian, X.; Miao, F.; Hui, F.; Shi, Y.; Larcher, L.; Wu, E.; Lanza, M. *Appl. Phys. Lett.* **2016**, *108*, 012905.

39. Coffey, D. C.; Reid, O. G.; Rodovsky, D. B.; Bartholomew, G. P.; Ginger, D. S. *Nano Lett.* **2007**, *7*, 738–744.

40. Guide, M.; Dang, X.-D.; Nguyen, T.-Q. *Adv. Mater.* **2011**, *23*, 2313–2319.

41. Son, Y.; Wang, Q. H.; Paulson, J. A.; Shih, C.-J.; Rajan, A. G.; Tvrdy, K.; Kim, S.; Alfeeli, B.; Braatz, R. D.; Strano, M. S. *ACS Nano* **2015**, *9*, 2843–2855.

42. Son, Y.; Li, M.-Y.; Cheng, C.-C.; Wei, K.-H.; Liu, P.; Wang, Q. H.; Li, L.-J.; Strano, M. S. *Nano Lett.* **2016**, *16*, 3571–3577.

43. Li, Y.; Xu, C.-Y.; Wang, J.-Y.; Zhen, L. *Sci. Rep.* **2014**, *4*, 7186.

44. Lee, H.; Deshmukh, S.; Wen, J.; Costa, V. Z.; Schuder, J. S.; Sanchez, M.; Ichimura, A. S.; Pop, E.; Wang, B.; Newaz, A. K. M. *ACS Appl. Mater. Interfaces* **2019**, *11*, 31543–31550.

45. Li, F.; Lu, Z.; Y.-W., L.; Jiao, L.; Xu, M.; Zhu, X.; Zhang, X.; Wu, H.; Qi, J. *Nanotechnology* **2018**, *29*, 275202.

46. Azulay, D.; Millo, O.; Balberg, I.; Schock, H.-W.; Visoly-Fisher, I.; Cahen, D. *Sol. Energy Mater Sol. Cells* **2007**, *91*, 85–90.

47. Brezna, W.; Strasser, G.; Smoliner, J. *Semicond. Sci. Technol.* **2007**, *22*, 1209–1212.

48. Ledinský, M.; Fejfar, A.; Vetushka, A.; Stuchlík, J.; Rezek, B.; Kočka, J. *Phys. Status Solidi - Rapid Res. Lett.* **2011**, *5*, 373–375.

49. Kratzer, M.; Rubezhanska, M.; Prehal, C.; Beinik, I.; Kondratenko, S. V.; Kozyrev, Y. N.; Teichert, C. *Phys. Rev. B* **2012**, *86*, 245320.

50. Ji, Y.; Hui, F.; Shi, Y.; Iglesias, V.; Lewis, D.; Niu, J.; Long, S.; Liu, M.; Hofer, A.; Frammelsberger, W.; Benstetter, G.; Scheuermann, A.; McIntyre, P. C.; Lanza, M. *Rev. Sci. Instrum.* **2016**, *87*, 083703.

51. Rahova, J.; Sampathkumar, K.; Vetushka, A.; Ledinsky, M.; Hajkova, Z.; Fejfar, A.; Frank, O. *Phys. Status Solidi B* **2018**, *255*, 1800305.

52. Wang, Q. H.; Kalantar-Zadeh, K.; Kis, A.; Coleman, J. N.; Strano, M. S. *Nat. Nanotechnol.* **2012**, *7*, 699–712.

53. Kang, J.; Tongay, S.; Zhou, J.; Li, J.; Wu, J. *Appl. Phys. Lett.* **2013**, *102*, 012111.

54. Duan, X.; Wang, C.; Pan, A.; Yu, R.; Duan, X. *Chem. Soc. Rev.* **2015**, *44*, 8859–8876.

55. Kufer, D.; Konstantatos, G. *Nano Lett.* **2015**, *15*, 7307–7313.

56. Fang, H.; Hu, W. *Adv. Sci.* **2017**, *4*, 1700323.

57. Han, P.; Adler, E. R.; Liu, Y.; Marie, L. S.; El Fatimy, A.; Melis, S.; Van Keuren, E.; Barbara, P. *Nanotechnology* **2019**, *30*, 284004.

58. Czerniak-Łosiewicz, K.; Gertych, A. P.; Świniarski, M.; Judek, J.; Zdrojek, M. *J. Phys. Chem. C* **2020**, *124*, 18741–18746.

59. Wang, H.; Wu, Y.; Cong, C.; Shang, J.; Yu, T. *ACS Nano* **2010**, *4*, 7221–7228.

60. Late, D. J.; Liu, B.; Matte, H. S. S. R.; Dravid, V. P.; Rao, C. N. R. *ACS Nano* **2012**, *6*, 5635–5641.

61. Lindvall, N.; Kalabukhov, A.; Yurgens, A. *J. Appl. Phys.* **2012**, *111*, 064904.

62. Rosenberger, M. R.; Chuang, H.-J.; McCreary, K. M.; Hanbicki, A. T.; Sivaram, S. V.; Jonker, B. T. *ACS Appl. Mater. Interfaces* **2018**, *10*, 10379–10387.